Mechanical Exfoliation of HOPG and Estimation of the Number of Layers of a Few Layered Graphene Flake

A summer internship report submitted in partial fulfillment of the requirements for the summer semester.

By

John Regis

Registration Number: 20246718

Internship Supervisor

Dr. Aparna Deshpande

Indian Institute of Science Education and Research

Abstract

Graphene, a single layer of carbon atoms arranged in a two-dimensional honeycomb lattice, has emerged as one of the most remarkable materials in modern science. Its exceptional electrical, mechanical, thermal, and optical properties make it a strong candidate for a wide range of technological applications from next-generation electronics and sensors to energy storage and quantum devices. The simplicity of its structure belies the complexity and depth of its physical behavior, offering a versatile platform for both theoretical exploration and experimental innovation.

Scanning probe techniques such as Scanning Tunneling Microscopy (STM) and Atomic Force Microscopy (AFM) have revolutionized the ability to probe surfaces at the nanoscale. While STM is particularly sensitive to electronic density of states and requires conductive samples, AFM provides topographical information with high spatial resolution regardless of conductivity. For atomically thin materials like graphene, AFM is particularly valuable, enabling precise measurement of height profiles and surface roughness. These techniques serve as indispensable tools in the structural and morphological characterization of two-dimensional materials.

The objective of this project was to mechanically exfoliate graphene from Highly Oriented Pyrolytic Graphite (HOPG) and identify monolayer flakes through topographical analysis. Using Atomic Force Microscopy (AFM), the height profile of exfoliated samples was examined to distinguish monolayer regions from multilayer counterparts. The presence of monolayer graphene was further confirmed through Raman spectroscopy, offering complementary spectroscopic validation of the flake thickness and structural integrity. A key aim of the internship was also to develop a foundational understanding of the theoretical principles behind Scanning Tunneling Microscopy (STM) and Atomic Force Microscopy (AFM), along with gaining hands-on experience in the practical operation of AFM instruments.

Table of Contents

Chapter 1

Introduction to STM and AFM

1 Overview of Scanning Probe Microscopy

Today, **quantum technology is one of the most important emerging fields**. We've already reached the physical limits of how small we can make transistors and how many we can fit onto a chip. To continue advancing, we need new technologies and a better understanding of the material world.

Across science and technology, there is a strong move toward working at extremely small scales right down to the atomic level. For instance, electronics is already shifting from microelectronics to nanoelectronics. Modern computers now include components so small that they can be considered true nanoelectronic devices.

This transition is also driven by the fact that the properties of materials are ultimately determined by their atomic structure. To truly understand how a material behaves, we must study it at the atomic or nanoscale. However, about fifty years ago, most people believed that directly accessing or interacting with individual atoms would be impossible.

1.1 Scanning Tunneling Microscopy (STM)

Scanning Tunneling Microscopy (STM) is a special method that allows **us** to see and study surfaces **one atom at a time**. It works based on the idea of *quantum tunneling*, where tiny particles like electrons can jump across a small gap between a sharp metal tip and a surface even when classical physics says they shouldn't.

In STM, a very sharp tip is brought extremely close to the surface we want to examine just a few atoms away. A small voltage is applied, and this causes a **tunneling current** to flow between the tip and the surface. This current is highly sensitive to the distance between the tip and the surface.

By carefully scanning the tip over the surface and measuring this current, we can map out the atomic structure.

STM operates in two main modes:

- **Constant Current Mode:** The tip moves up and down to keep the tunneling current constant as it scans the surface. The vertical motion of the tip provides information about the surface structure. This mode gives highly detailed images but takes more time.
- **Constant Height Mode:** The tip stays at a fixed height while the tunneling current is measured as it changes over the surface. This mode is faster and useful for very flat surfaces but may lose detail if the surface has large height variations.

To get accurate results, STM is usually performed under **ultrahigh vacuum** and at **low temperatures**, which help avoid disturbances from air and thermal vibrations.

1.2 Physics of STM

Scanning Tunneling Microscopy (STM) operates on the principle of *quantum tunneling*, a non-classical phenomenon wherein electrons can traverse a potential barrier that they would not be able to cross according to classical mechanics. This mechanism enables STM to achieve atomic-level resolution of surfaces.

To gain a deeper understanding of the physics behind STM, I consulted two authoritative texts: *Introduction to Scanning Tunneling Microscopy* by Julian Chen and *Scanning Probe Microscopy* by Bert Voigtländer. These works provide the theoretical framework and mathematical formalism that underpin the operation of STM.

In STM, a conductive tip is positioned extremely close—on the order of a few angstroms—to the sample surface. When a bias voltage is applied between the tip and the sample, electrons can tunnel through the vacuum gap, giving rise to a measurable **tunneling current**. This current is highly sensitive to the tip-sample separation and is governed by the quantum mechanical transmission probability.

By solving the time-independent Schrödinger equation for a one-dimensional rectangular potential barrier, one obtains an expression for the **tunneling**

transmission coefficient T:

$$T \approx e^{-2\kappa d} \quad where \quad \kappa = \frac{\sqrt{2m(\phi - E)}}{\hbar}$$

Here, d is the tip-sample separation, m is the electron mass, ϕ is the effective barrier height (typically related to the average of the work functions of the tip and the sample), E is the energy of the tunneling electron, and $\hbar$ is the reduced Planck constant.

This exponential dependence of T on the distance d accounts for STM's extreme sensitivity to atomic-scale variations in surface height. Even a change of a fraction of an angstrom in the separation can lead to an order-of-magnitude variation in the tunneling current. Thus, the current provides a direct probe of the local electronic density of states near the Fermi level.

The expressions and physical interpretations drawn from the texts by Chen and Voigtländer form the basis of understanding how STM captures electronic and topographic information with sub-nanometer resolution.

One of the most important theoretical frameworks for understanding tunneling in STM is the Landauer theory of tunneling. This model provides a quantitative relationship between the tunneling current and the quantum mechanical transmission probability of electrons across a potential barrier. As discussed in the book by Julian Chen, this theory treats conductance as a transmission problem, where the tunneling barrier acts as a quantum filter for electrons.

In the context of STM, electrons tunnel from the tip to the sample or from the sample to the tip depending on the direction of the applied bias voltage. The Landauer approach expresses the tunneling current as an integral over energy, weighted by the difference in the Fermi-Dirac distribution functions of the tip and the sample, and modulated by the transmission probability.

The expression for the tunneling current is given by:

$$I = \frac{2e}{h} \int_{-\infty}^{\infty} T(E) \left[f(E - eV) - f(E) \right] \, dE$$

Here, I is the tunneling current, e is the elementary charge, h is Planck's constant, $T(E)$ is the energy-dependent transmission probability, $f(E)$ is the Fermi-Dirac distribution function, and V is the applied bias voltage.

This expression reflects the idea that only electrons near the Fermi level

contribute significantly to the tunneling current, as those are the ones that experience a difference in occupancy between the tip and the sample.

In the low-temperature and small-bias limit, this integral simplifies, and the current becomes approximately linear in V. The resulting expression is:

$$I \approx \frac{2e^2}{h} T(E_F) V$$

where E_F is the Fermi energy. This simplified form shows that the tunneling current is directly proportional to the transmission probability at the Fermi level and to the applied voltage.

Landauer's theory provides a clear physical picture of how quantum transport occurs in STM. It shows that electrical conduction at the nanoscale is not just a material property but arises from the probability of quantum states connecting across the tunneling junction. Another fundamental approach to understanding tunneling in STM is Bardeen's theory of tunneling. This method is based on time-dependent perturbation theory and provides a microscopic quantum mechanical derivation of the tunneling current. Bardeen treated the tip and sample as two separate systems, each with its own set of eigenstates, and calculated the tunneling current by evaluating the overlap between these states.

In this model, the tunneling current arises from the transition of electrons from occupied states in one electrode to unoccupied states in the other, mediated by a tunneling matrix element. The probability of tunneling is determined by Fermi's golden rule, applied using the overlap of wavefunctions across the barrier.

The expression for the tunneling current in Bardeen's formulation is:

$$I = \frac{4\pi e}{\hbar} \sum_{\mu,\nu} \left[f(E_\mu) - f(E_\nu) \right] \left| M_{\mu\nu} \right|^2 \delta(E_\mu - E_\nu)$$

In this expression, I is the tunneling current, e is the elementary charge, $\hbar$ is the reduced Planck constant, $f(E)$ is the Fermi-Dirac distribution function, E_μ and E_ν are the energies of states in the tip and sample respectively, and $M_{\mu\nu}$ is the tunneling matrix element between state μ in the tip and state ν in the sample.

The delta function $\delta(E_\mu - E_\nu)$ ensures energy conservation in the tun-

neling process, meaning only those states with equal energy can contribute to the current.

The matrix element $M_{\mu\nu}$ itself is given by an integral over a surface S in the vacuum gap:

$$M_{\mu\nu} = \frac{\hbar^2}{2m} \int_S \left(\psi_\mu^* \nabla \psi_\nu - \psi_\nu \nabla \psi_\mu^* \right) \cdot d\mathbf{S}$$

where ψ_μ and ψ_ν are the wavefunctions of the tip and sample states respectively, and m is the electron mass. This integral quantifies the overlap of the wavefunctions from the two electrodes across the vacuum barrier.

Bardeen's theory is particularly powerful because it provides a way to calculate tunneling current based on the electronic structures of the tip and sample. It forms the theoretical foundation for many modern simulations of STM and scanning probe microscopy in general.

1.3 Atomic Force Microscopy

Atomic Force Microscopy (AFM) is another powerful technique that allows **us** to see surfaces at the level of atoms. Unlike STM, which depends on electron tunneling, AFM works by physically *touching* the surface with a tiny, sharp tip that is attached to a flexible cantilever.

As the tip moves over the surface, it experiences very small forces (like van der Waals forces or electrostatic forces) from the atoms on the surface. These forces cause the cantilever to bend slightly. A laser beam is reflected off the back of the cantilever onto a position-sensitive detector to measure this bending.

AFM can work in different modes depending on how the tip interacts with the surface. The two most common modes are:

- **Contact Mode:** In this mode, the tip touches the surface gently while scanning. The deflection of the cantilever is monitored to map the surface. It gives high-resolution images but may damage soft samples due to continuous contact.
- **Tapping Mode (also called Intermittent Contact):** Here, the cantilever is made to oscillate up and down, and the tip only briefly touches the surface at each cycle. This reduces damage to delicate surfaces and is widely used for biological and soft materials.

In this project, most of the surface analysis has been done using AFM in the **dynamic (tapping) mode**, specifically for *height measurement and surface mapping*.

1.4 Physics of Tapping Mode in AFM

In this section, we discuss only the tapping mode of operation in Atomic Force Microscopy (AFM), as it is the mode relevant to our project. Other modes, such as contact or non-contact mode, are not included in this discussion.

The working of tapping mode can be understood by first considering the nature of the interaction between the AFM cantilever tip and the sample surface. These interactions are often described using the Lennard-Jones potential, which models the force between a pair of atoms or molecules as a function of their separation. The potential is given by the expression:

$$U_{LJ}(r) = 4U_0 \left[\left(\frac{R_a}{r} \right)^{12} - \left(\frac{R_a}{r} \right)^{6} \right]$$

Here, U_0 represents the depth of the potential well, R_a is the distance at which the potential is minimum (often referred to as the equilibrium separation), and r is the instantaneous distance between the tip and the sample surface. The term $\left(\frac{R_a}{r}\right)^{12}$ corresponds to the short-range repulsive interactions due to overlapping electron clouds, while $\left(\frac{R_a}{r}\right)^{6}$ describes the long-range attractive van der Waals interactions.

In tapping mode, the cantilever oscillates close to its resonant frequency, and it interacts intermittently with the surface, primarily operating in the attractive regime of the Lennard-Jones potential. The amplitude and phase of the cantilever's oscillation change depending on the nature of the surface beneath it. These variations are used to reconstruct the topography of the sample. Because the tip only intermittently contacts the surface, tapping mode reduces damage to both the tip and the sample, making it ideal for imaging soft or fragile surfaces.

For our project, we exclusively used tapping mode for imaging. We did not employ contact mode for regular scanning purposes. However, to remove any impurities or particles picked up by the AFM tip, we used contact mode briefly as a cleaning step. In this cleaning procedure, we switched

the AFM into contact mode and scanned a clean Si/SiO_2 surface along just three lines. This was sufficient to dislodge impurities from the cantilever tip without damaging it or the surface. There is an effect called snap-to-contact or snapping, which can occur during Atomic Force Microscopy measurements. This effect can be understood using a simple analogy involving a magnet and an iron plate. Imagine a magnet hanging from a spring. As an iron plate is slowly brought closer, the magnet experiences a weak attractive force and shifts slightly. However, once the plate is too close, the magnetic force overcomes the restoring force of the spring, causing the magnet to suddenly snap onto the plate. In AFM, a similar situation occurs when the attractive interaction between the cantilever tip and the sample surface becomes stronger than the cantilever's restoring force. The tip then abruptly jumps into contact with the surface, which can lead to loss of imaging control or even damage. To avoid this, a technique called tapping mode is used, where the cantilever is driven to oscillate such that the tip interacts intermittently with the surface. This brief and controlled interaction reduces the chances of the tip sticking to the sample. In our measurements, we used only tapping mode for imaging to prevent this issue. Contact mode was used just once for the purpose of cleaning the tip by scanning a few lines on a clean Si/SiO_2 substrate.

Chapter 2

Proportional-Integral-Derivative (PID) Control System

2 Overview of PID Control

The reason an entire chapter is dedicated to the PID control system in this internship report is due to its central role during the operation of the Atomic Force Microscope (AFM) while imaging graphene flakes. Throughout the experiment, the PID parameters were frequently adjusted to minimize noise and achieve clear, noiseless images. Fine-tuning these settings was critical for obtaining reliable imaging data. Given its direct impact on the image quality and experimental success, the PID control system deserved focused attention and discussion, as it was not just a background mechanism but a tool I actively engaged with during the internship. Control systems are used everywhere from household appliances like air conditioners to advanced machines like satellites. At the heart of many of these systems is something called a feedback loop.

Feedback is the idea of measuring what a system is doing and using that information to improve its performance. Imagine driving a car: if you see the car drifting to the left, you quickly steer to the right. That visual information (feedback) helps you stay on track.

In engineering systems, feedback does the same job. It helps us adjust a system's behavior based on how it's performing. If a motor is running too slowly, feedback tells the controller to speed it up. If it's going too fast, feedback helps slow it down.

This is where the **PID controller** comes in. It stands for Proportional Integral Derivative, and it's a method used to continuously calculate the correction needed to make a system do what we want. It takes into account:

- How far we are from the target (Proportional)

- How long we've been off target (Integral)
- How fast the error is changing (Derivative)

Together, these three parts make the PID controller very powerful. It helps machines work smoothly, accurately, and automatically — without needing someone to constantly adjust things.

2.1 Proportional Control

Proportional control is the first and most basic part of a PID controller. The idea is very simple: the bigger the error, the stronger the response.

In any control system, we define an **error** as the difference between what we want (the *setpoint*) and what we actually get (the *process variable*). Proportional control works by multiplying this error by a constant value, called the **proportional gain** (K_p).

$$u(t) = K_p \cdot e(t) \tag{1}$$

Where:

- $u(t)$ is the control signal (the output of the controller)
- K_p is the proportional gain (a constant that determines how aggressive the response is)
- $e(t)$ is the error at time t (i.e., $e(t) = Setpoint - ProcessVariable$)

This means that if the error is large, the control signal will also be large. If the error is small, the control signal will be small. In this way, the system reacts in proportion to how far off it is from the target.

Example: Think of a room heater. If the room is much colder than the desired temperature, the heater will turn on at a high level. As the temperature gets closer to the desired value, the heater reduces its output.

However, proportional control alone often leaves a small steady error, called the *offset*, which is why we also need Integral and Derivative parts — discussed next.

While proportional control is simple and effective, it has a major drawback: **it usually cannot eliminate the error completely**. This leftover error is called the **steady-state error** or **steady-state deviation**.

Here's what happens:

- When there is a big error, the proportional control produces a strong response — good!
- But as the system gets closer to the desired value, the error becomes smaller.
- That means the control signal also becomes weaker.

Eventually, the system reaches a point where the control output is *too small* to push the system any closer to the target. It stops improving — and you're left with a small but permanent gap between the setpoint and the actual value.

Example: Imagine you're trying to push a heavy box to a certain spot. If you always push in proportion to how far it is from the target, you'll start strong but slow down as you get closer. At some point, your push is so weak that friction takes over, and the box just stops slightly short of the target. This is why proportional control *alone* is often not enough in precise systems. To fix this issue and eliminate the steady-state error, we add an **integral component**, which keeps track of the error over time and forces the system to eventually reach the exact target that's coming up next.

2.2 Integral Control

To solve the problem of steady-state error in proportional control, we add something called an **Integral Control**.

The idea is simple: instead of just reacting to the present error, we also look at the **history of all past errors**. The longer the error stays, the more the controller builds up a response.

In simple words: Integral control keeps adding up the error over time and uses this total (or "accumulated") error to push the system harder toward the target.

Mathematical expression:

$$u(t) = K_I \int_0^t e(\tau)\, d\tau$$

Where:

- $u(t)$ is the control output,
- K_I is the integral gain,
- $e(\tau)$ is the error at time τ,
- The integral sums up the error from time 0 to current time t.

It eliminates the steady-state error completely — because even a small leftover error will keep getting added up, making the controller push harder until the error is gone. But there's a problem: This method can sometimes overreact. If the error builds up too much, the system may overshoot or become unstable.The solution? Add Derivative Control. To smooth things out and avoid overshooting, we introduce a third part: the Derivative Control, which looks at how fast the error is changing and slows things down when needed.

2.3 Derivative Control

Derivative control acts like a predictor — it considers how quickly the error is changing with time and attempts to counteract this trend. This helps in reducing overshoot and adds damping to the system response, especially during sudden changes. It is particularly useful for improving the stability and transient behavior of a control system.

The mathematical expression for the derivative control action is:

$$u_D(t) = K_D \frac{de(t)}{dt} \tag{2}$$

where:

- $u_D(t)$ is the derivative control output,
- K_D is the derivative gain,
- $\frac{de(t)}{dt}$ is the rate of change of error with respect to time.

2.4 Complete PID Control Expression

The full PID (Proportional-Integral-Derivative) control law is a combination of three terms proportional to the present error, integral of past errors, and derivative of the future trend of the error. The expression is given as:

$$u(t) = K_P e(t) + K_I \int_0^t e(\tau)\, d\tau + K_D \frac{de(t)}{dt} \tag{3}$$

where:

- $u(t)$ is the total control signal,
- $e(t)$ is the instantaneous error signal at time t,
- K_P is the proportional gain,
- K_I is the integral gain,
- K_D is the derivative gain.

This combination ensures that the system responds quickly (proportional), corrects steady-state errors (integral), and anticipates future errors (derivative), thereby enabling precise and stable control — essential for tasks like achieving noiseless AFM images.

Chapter 3

Quantum Technology Workshop IISc Bangalore

3 Talks and Lab Visits in IISc Bangalore

The workshop organized by QuRP at IISc Bangalore turned out to be very helpful. At first, I thought it would be limited in scope, but it included a wide range of talks, especially from professors working with 2D materials. This gave me a better understanding of topics related to my interests.One talk I found interesting was about a material called indium selenide. The speaker explained how this material can switch between two forms — amorphous and crystalline — which can be used to represent 0 and 1 in classical computers. It was exciting to learn that materials like this could be used for future data storage.

Another talk explained the hot injection method used to make quantum dots. By changing their size, we can control their color and energy levels. These dots are useful for making single-photon sources, which are important in quantum communication. We also got to visit some labs. One lab session was on Raman spectroscopy. A professor gave us a tour and showed how this method can be used to tell the difference between graphene and graphite. Seeing how the theory is applied in real experiments made the learning experience much richer.Overall, the workshop was a great mix of theory and hands-on learning. It gave me new ideas and a better understanding of how research is done in real labs.

Chapter 4

Raman Spectroscopy

4 General Overview of Raman Spectroscopy

To estimate the number of graphene layers, we often use Atomic Force Microscopy (AFM), and to confirm the results, Raman spectroscopy is also used. That's why it is important to understand the basic ideas behind Raman spectroscopy. To learn more, I read a few research papers that explain how Raman spectra can be interpreted, especially for graphene, and I've noted down the important points from those readings

Raman spectroscopy is a useful and widely used method to study materials without damaging them. It is especially helpful in both laboratories and real-world settings. This technique was first developed in the early 20th century by scientists C. V. Raman and G. S. Landsberg. However, it became more commonly used after lasers were introduced later in the century. Raman spectroscopy helps scientists understand materials in greater detail, especially carbon-based ones like graphite. Over time, it has become valuable in many industries, including food and textiles. Compared to other methods like infrared spectroscopy, Raman spectroscopy has some key benefits — for example, water does not interfere much with the results, which makes it suitable in situations where other methods fail. It has even been successfully used to monitor processes like fermentation in real-time. Still, it has some challenges, such as difficulty in analyzing the data accurately and the problem of certain strong signals, like those from carbon particles, hiding other signals. Researchers are actively working to solve these issues. This review looks at how Raman spectroscopy is used to study different materials and explains the science behind how it works, helping readers understand its broad potential and current developments.

When light interacts with matter, it can be absorbed, passed through (transmitted), or scattered. Absorption happens when the energy of the

light exactly matches the energy gap between two electronic states. Scattering, however, does not need this energy match as it happens when light hits a molecule and briefly disturbs its electrons, creating what is called a virtual state. This state does not last long, and the system returns to a real energy level and releases a photon. If the released photon has the same energy as the incoming one, it is called Rayleigh scattering which is also known as elastic scattering. But if the energy changes either increasing or decreasing, it is called Raman scattering which is also known as inelastic scattering. When the scattered photon has less energy, it is called a Stokes shift, and if it has more energy, it is called an anti Stokes shift. The difference in energy is known as the Raman shift. The strength of Raman signals also depends on how the molecules are distributed across energy levels, which follows a rule called the Boltzmann distribution. At room temperature, more molecules are in the ground state, so Stokes scattering is stronger than anti Stokes. If the incoming light matches a real energy level, the signal is much stronger and this is called Resonance Raman scattering. Still, Raman scattering is very weak overall and only about one in one hundred million photons shows this effect, so instruments use filters to remove stronger background signals like Rayleigh scattering. The intensity of the Raman signal also depends on factors like the number of molecules, the incoming light intensity and frequency, and how easily the molecule's electrons can be disturbed which is known as polarizability. However, using higher energy light to increase signal strength can also damage the sample, so there is a trade off to consider in real applications.

4.1 Graphene and Graphene-Like Materials

The Raman spectrum of single layer graphene has two main peaks: the G peak around 1582 cm^{-1} and the 2D peak around 2700 cm^{-1}. These peaks help us study the structure of the graphene sheet. Graphene with defects also shows a D peak, which mainly appears at armchair edges due to how light scatters. Zigzag edges show a weaker D peak because of their shape and surface roughness.

Temperature also affects the Raman bands. At lower temperatures, the G band splits, and at higher temperatures, its position shifts downward. These changes reverse when the sample is heated and cooled. The number

of layers in a graphene sample can be estimated by comparing the height of the G and 2D peaks. A high G to 2D ratio suggests more layers. The shape and position of these peaks also change depending on how many layers there are because the electronic structure and vibrations evolve. Some studies use the G peak and the silicon peak in the Raman spectrum to count atomic layers on a silicon surface. Others have explored how certain chemicals like PMMA affect the strain in graphene and shift its Raman peaks.One interesting finding is that the width of the 2D peak becomes narrower when the electron mobility is higher. The D to G peak ratio however stays the same. This means Raman spectroscopy can help study how well electrons move in graphene. In summary the G D and 2D peaks in the Raman spectrum give valuable information about the structure thickness defects and electronic behavior of graphene.

In the Raman spectrum, graphene exhibits a single sharp 2D peak at around 2700 cm^{-1} that is significantly more intense than the G peak at 1580 cm^{-1}, with the 2D intensity roughly four times that of the G peak. In contrast, graphite shows a broader and weaker 2D band, split into two components and having only about half the intensity of the G peak. The shape and intensity of the 2D peak are strong indicators of the number of layers: single-layer graphene has a single symmetric 2D peak, bilayer graphene shows a broader 2D band with four components, and multilayer graphene gradually resembles bulk graphite. The D peak, which appears at edges or in the presence of disorder, is absent in the central region of the sample, confirming minimal defects. These features allow Raman spectroscopy to reliably identify the number of graphene layers and their structural properties.

Chapter 5

Preparation of Samples

5 Preparation of Samples Using Mechanical Exfoliation

For atomic force microscopy (AFM) imaging, the choice and cleanliness of the substrate are crucial. Two commonly used substrates are silicon with a silicon dioxide layer (Si/SiO_2) and mica. These are selected because they provide an atomically flat surface that helps in obtaining accurate and high-resolution images. Si/SiO_2 substrates are especially useful for identifying graphene layers due to the optical contrast it provides under a microscope. Mica, on the other hand, can be cleaved easily to expose a clean and smooth surface, making it suitable for various types of imaging and deposition.

Cleaning the substrate is an essential step before imaging. If the surface contains dust, oils, or leftover adhesive, it can lead to poor-quality AFM images. During my own imaging sessions, I observed that improper cleaning caused the AFM tip to pick up glue or other contaminants. This led to increased background noise and even distorted the surface topology, making the measurements unreliable. After switching to a strict cleaning protocol, these issues were significantly reduced, and the imaging quality improved considerably.

5.1 Cleaning Protocol for Si/SiO_2 Substrates

The standard procedure we followed involves a three-step solvent cleaning process. Each step is designed to remove different types of contaminants from the substrate surface.

1. **Sonication in Acetone (10 minutes):** The substrate is first placed in a beaker of acetone and sonicated for 10 minutes. Acetone is effective in dissolving organic materials and adhesives that may be present on the surface.

2. **Sonication in Isopropanol (10 minutes):** After acetone cleaning, the substrate is transferred to a fresh beaker containing isopropanol (IPA) and again sonicated for 10 minutes. This step removes any acetone residue and also helps eliminate finer organic contaminants.

3. **Rinse and Drying:** Finally, the substrate is rinsed thoroughly with deionized water to remove any remaining solvent. After rinsing, it is blown dry using nitrogen gas. This prevents watermarks and ensures the surface remains clean until use.

By following this procedure carefully, we can achieve a clean and stable surface suitable for AFM measurements. This greatly reduces the risk of contamination and noise during the scanning process.

5.2 Mechanical Exfoliation of Highly Oriented Pyrolytic Graphite (HOPG)

Mechanical exfoliation is a widely used method to isolate thin layers of graphene from bulk graphite, particularly from highly ordered pyrolytic graphite (HOPG). In this process, adhesive tape is used to repeatedly peel layers from the bulk material and subsequently transfer the thinned flakes onto a clean substrate.

In our case, we chose to use blue tape instead of conventional Scotch tape or other commercial adhesive tapes. Blue tape is known to leave less adhesive residue and provides better exfoliation yield in terms of clean, thin flakes. The exfoliation procedure we followed is detailed below:

1. **Taping the HOPG:** A fresh piece of HOPG was gently pressed onto the surface of a piece of blue tape. The tape was folded over the HOPG to cover it entirely and then pressed slightly to ensure good contact between the tape and the graphite.

2. **Repeated Peeling:** The tape with HOPG was unfolded and folded multiple times, each time peeling the graphite apart. This reduces the flake thickness with each iteration and increases the chance of obtaining monolayer or few-layer graphene.

3. **Heat-Assisted Transfer:** After thinning the flakes, the tape with exfoliated graphite was pressed onto a pre-cleaned Si/SiO_2 substrate. The tape-substrate assembly was then placed on a hot plate at 90C for 5

minutes. Heating helps soften the adhesive and improves the adhesion of the flakes to the substrate.

4. **Transfer to Substrate:** After heating, the tape was gently peeled off. During this process, thin flakes from the HOPG are transferred onto the Si/SiO_2 surface.

5. **Optical Inspection:** The substrate was then inspected under an optical microscope to locate regions with thin flakes. These regions were noted for further analysis using AFM and Raman spectroscopy.

This method is simple, cost-effective, and provides good quality samples suitable for preliminary studies. However, successful exfoliation depends heavily on factors like tape type, cleanliness of the substrate, and the exfoliation pressure applied. The use of blue tape and mild heating significantly improved our yield of usable graphene flakes compared to standard methods.

Chapter 6

Height Profile Analysis using AFM

6 AFM imaging of selected Flakes

After identifying a few selected graphene flakes on the substrate, we performed Atomic Force Microscopy (AFM) scanning to analyze their thickness. The AFM image provides a height profile of the flake, which helps estimate the number of graphene layers present. Since a single layer of graphene typically has a thickness of about 0.345 nanometers, we can compare the measured height with this reference to determine how many layers are in the sample. Using this approach, we conducted AFM analysis for three different flakes.

6.1 Analysis of Flake 1

The AFM image of the first selected flake is shown below. Although the image quality was relatively poor and contained significant noise, it was still possible to perform a basic height analysis. By using an image processing software called SPIP, the image was enhanced to some extent, and the height profile of the flake was extracted for further evaluation.

A zoomed-in AFM scan was performed for improved height analysis. The corresponding height profile and the height analysis is shown below.

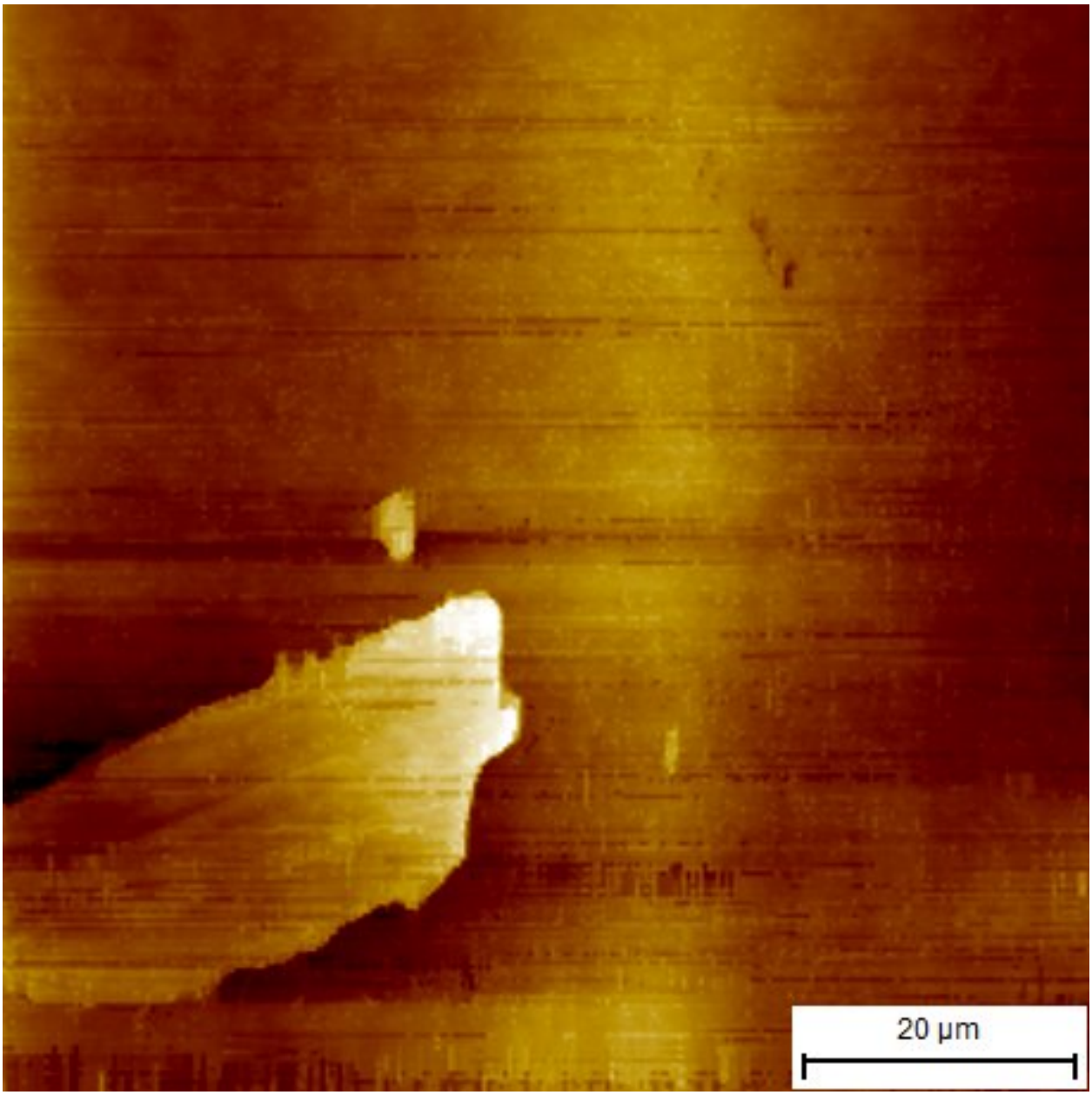

Figure 1: AFM image of the first selected flake. The scan size is 80µm × 80µm Before processing

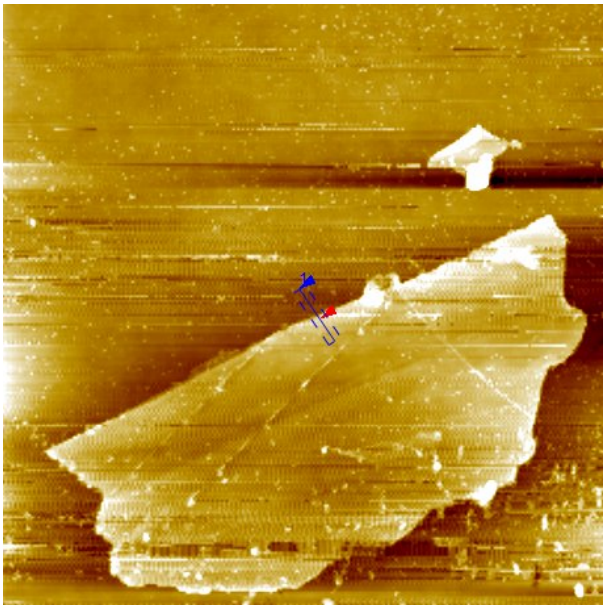

(a) AFM image of the selected flake.Selected cross section, averaged to nearly 5 lines

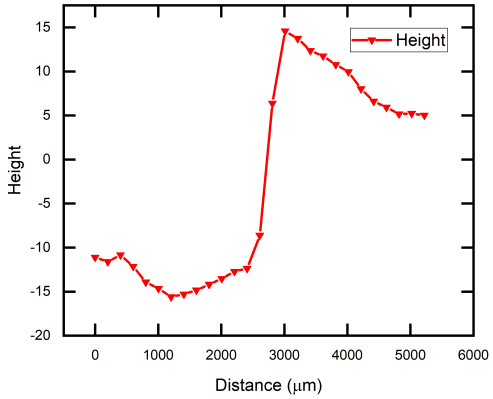

(b) Height analysis corresponding to the AFM image.

Figure 2: AFM image of the selected flake.Selected cross section, averaged to nearly 10 lines

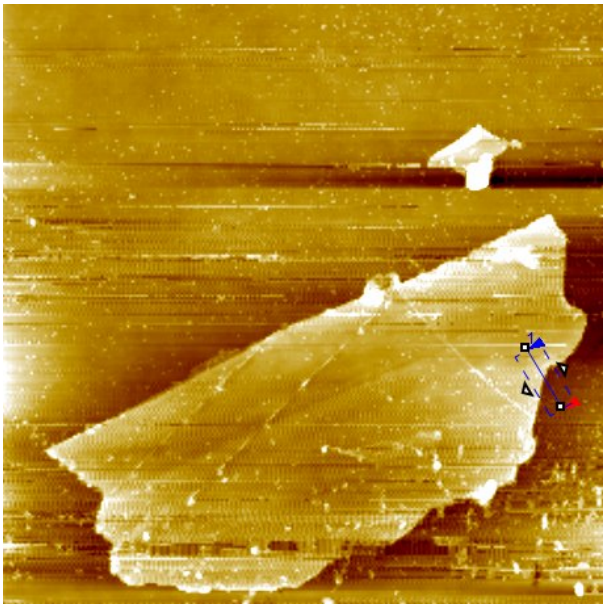

(a) AFM image of the selected flake.

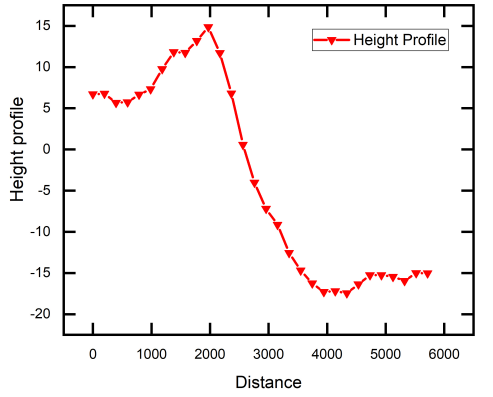

(b) Height analysis corresponding to the AFM image.

Figure 3: AFM image and height analysis of the selected graphene flake.

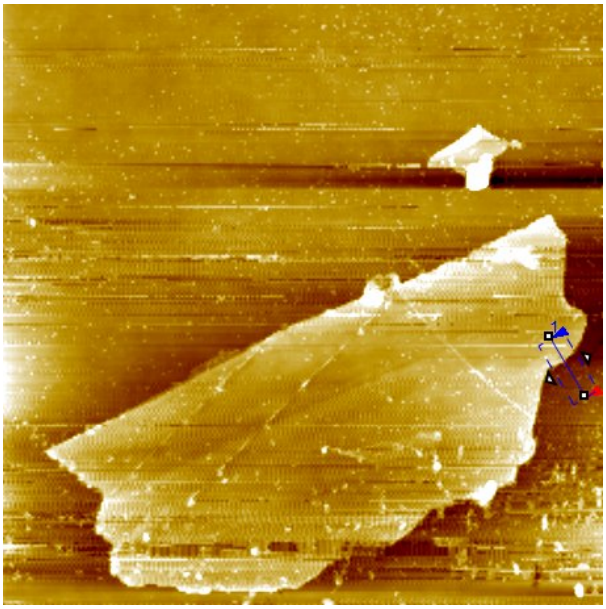

(a) AFM image of the selected flake.

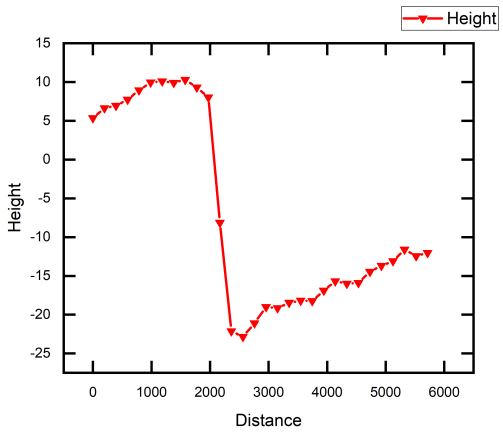

(b) Height analysis corresponding to the AFM image.

Figure 4: AFM image and height analysis of the selected graphene flake.

Since the image was too noisy, it was difficult to determine a consistent height across the flake. Therefore, a second flake was selected for further analysis.

6.2 Analysis of Flake 2

A second flake was identified, and the same analysis was repeated. An AFM scan was taken, and the height of the flake was analysed using SPIP software. The AFM image along with the corresponding height analysis is shown below.

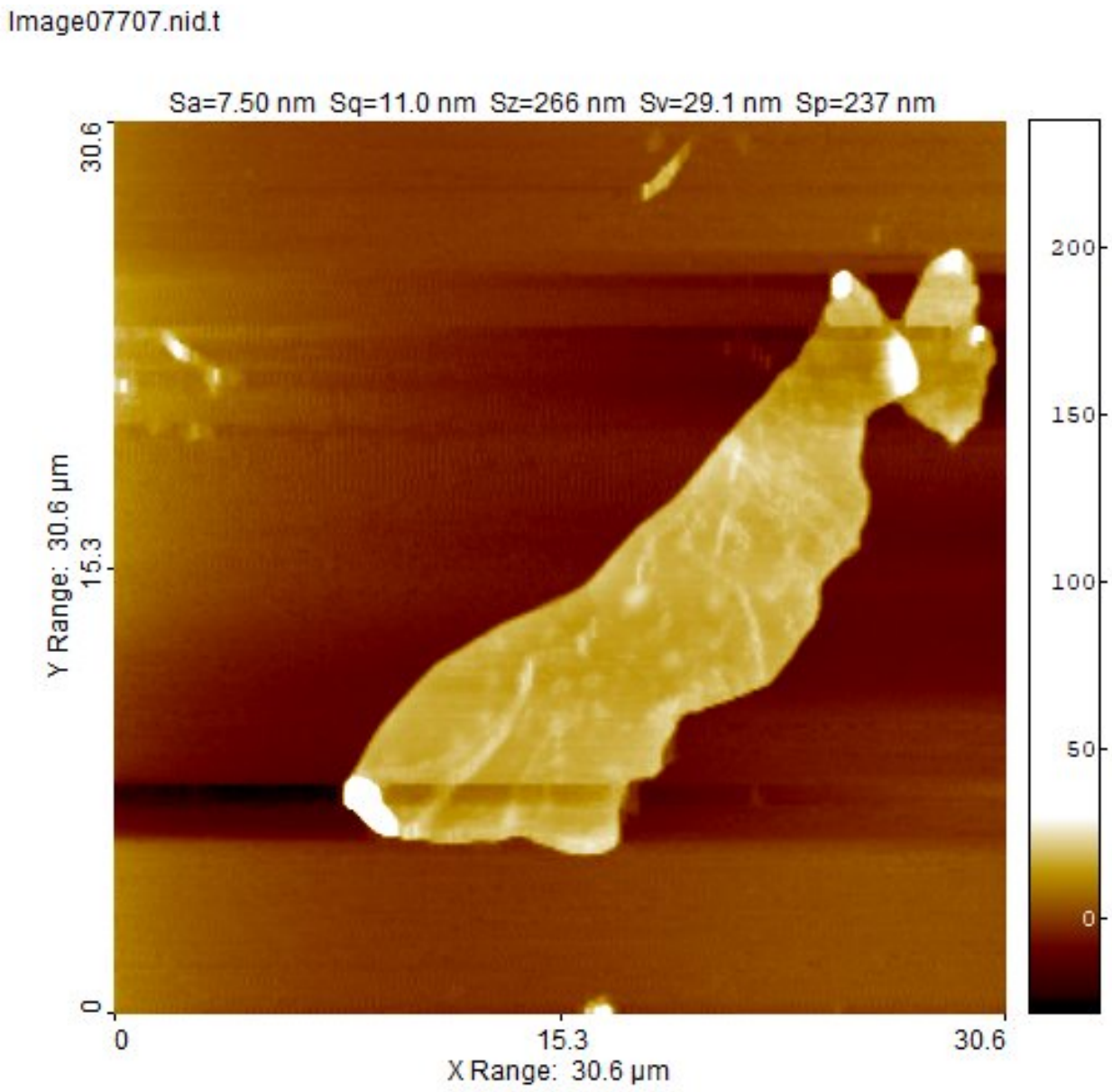

Figure 5: AFM image of the second selected flake. The scan size is 80.6µm × 30.6µm Before processing

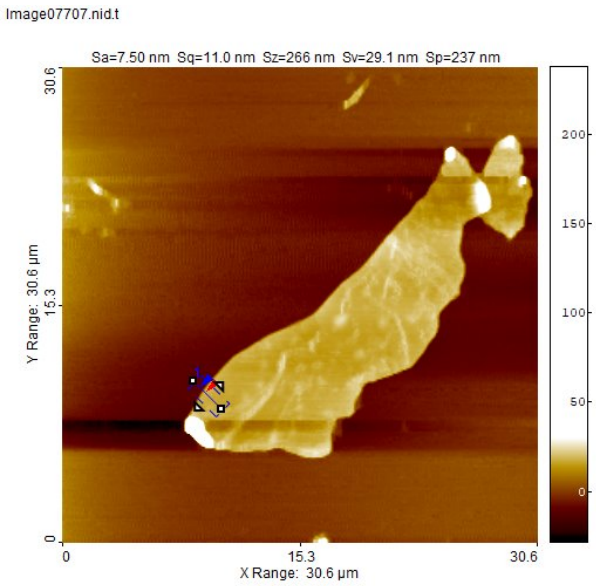

(a) AFM image of the selected flake.

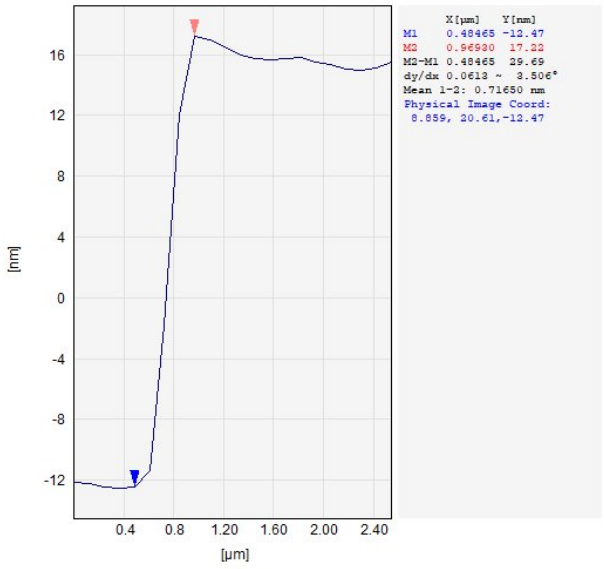

(b) Height analysis corresponding to the AFM image.

Figure 6: AFM image and height analysis of the selected graphene flake.

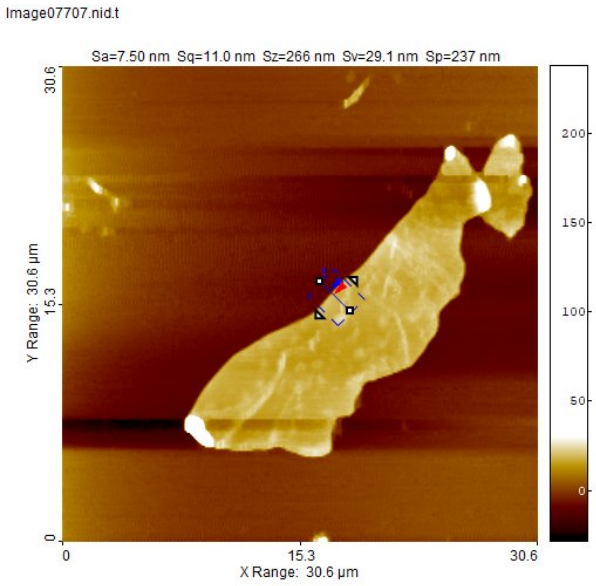

(a) AFM image of the selected flake.

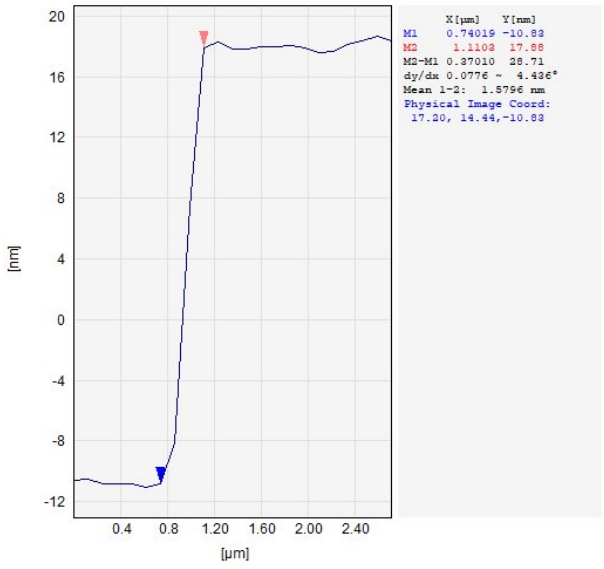

(b) Height analysis corresponding to the AFM image.

Figure 7: AFM image and height analysis of the selected graphene flake.

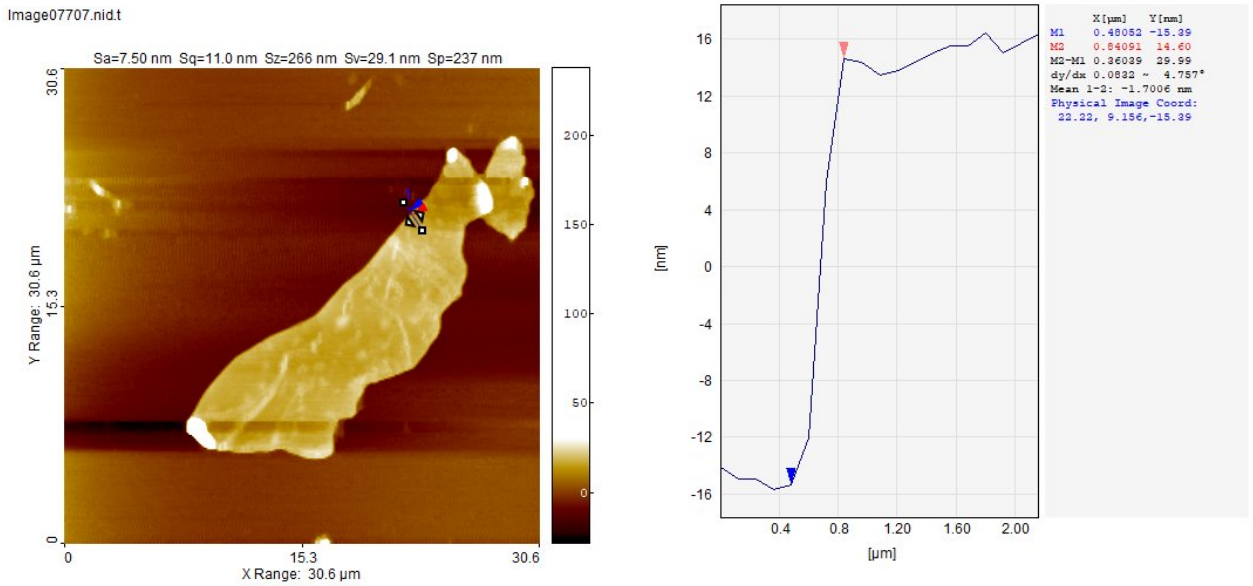

(a) AFM image of the selected flake.

(b) Height analysis corresponding to the AFM image.

Figure 8: AFM image and height analysis of the selected graphene flake.

In this analysis, a significantly large step height was observed, indicating that the flake is composed of multilayer graphene rather than a single or few-layer structure. Height measurements taken at six different cross-sections revealed that the flake is approximately 30nm thick, corresponding to roughly 88 graphene layers.

6.3 Analysis of the third Flake

A third flake was identified, with an aim to select a very thin and nearly transparent region in the hope that it would be a monolayer. The AFM image, corresponding height analysis, and the optical image are shown below.

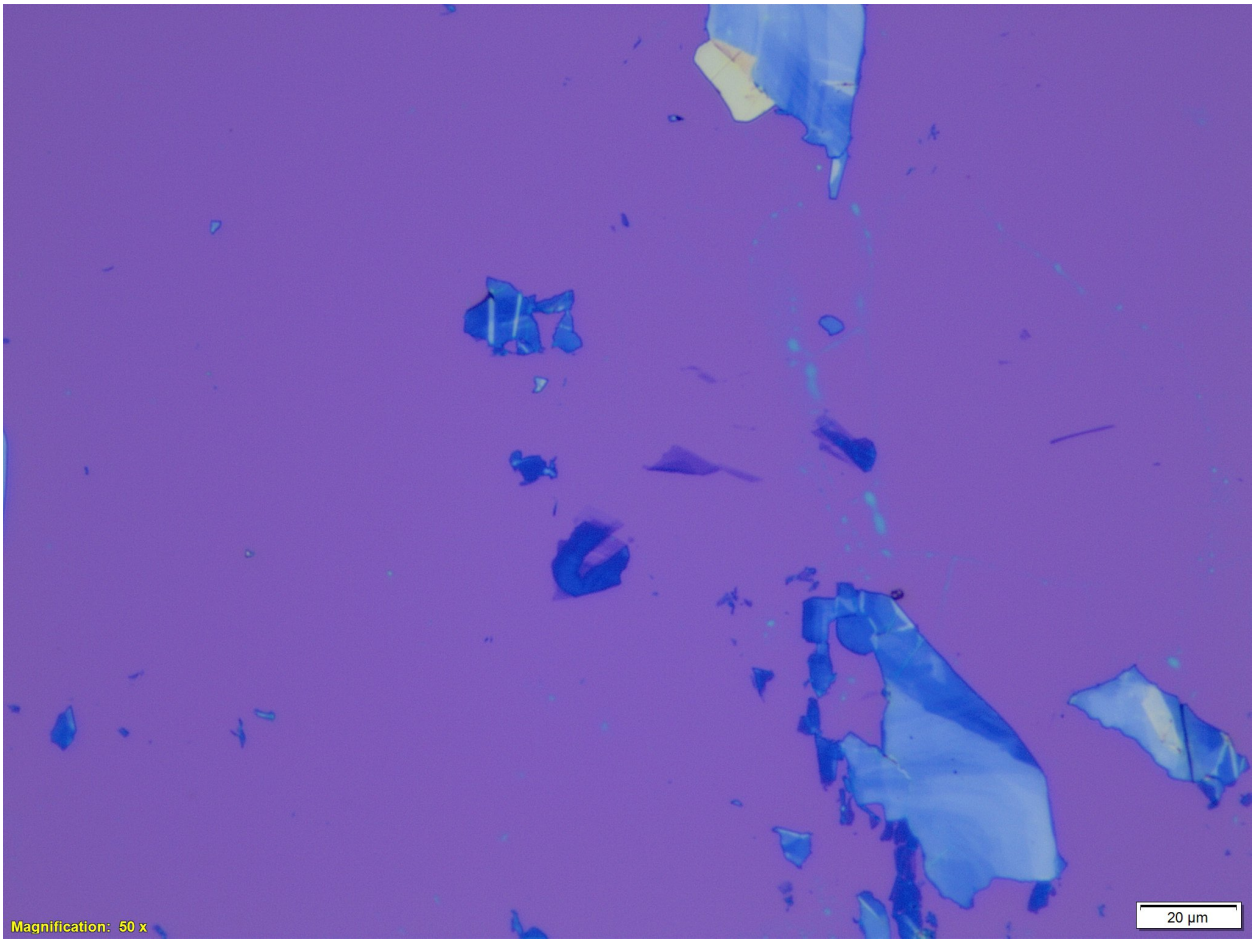

Figure 9: Optical Microscope image of the third selected flake.The flake is exactly at the centre

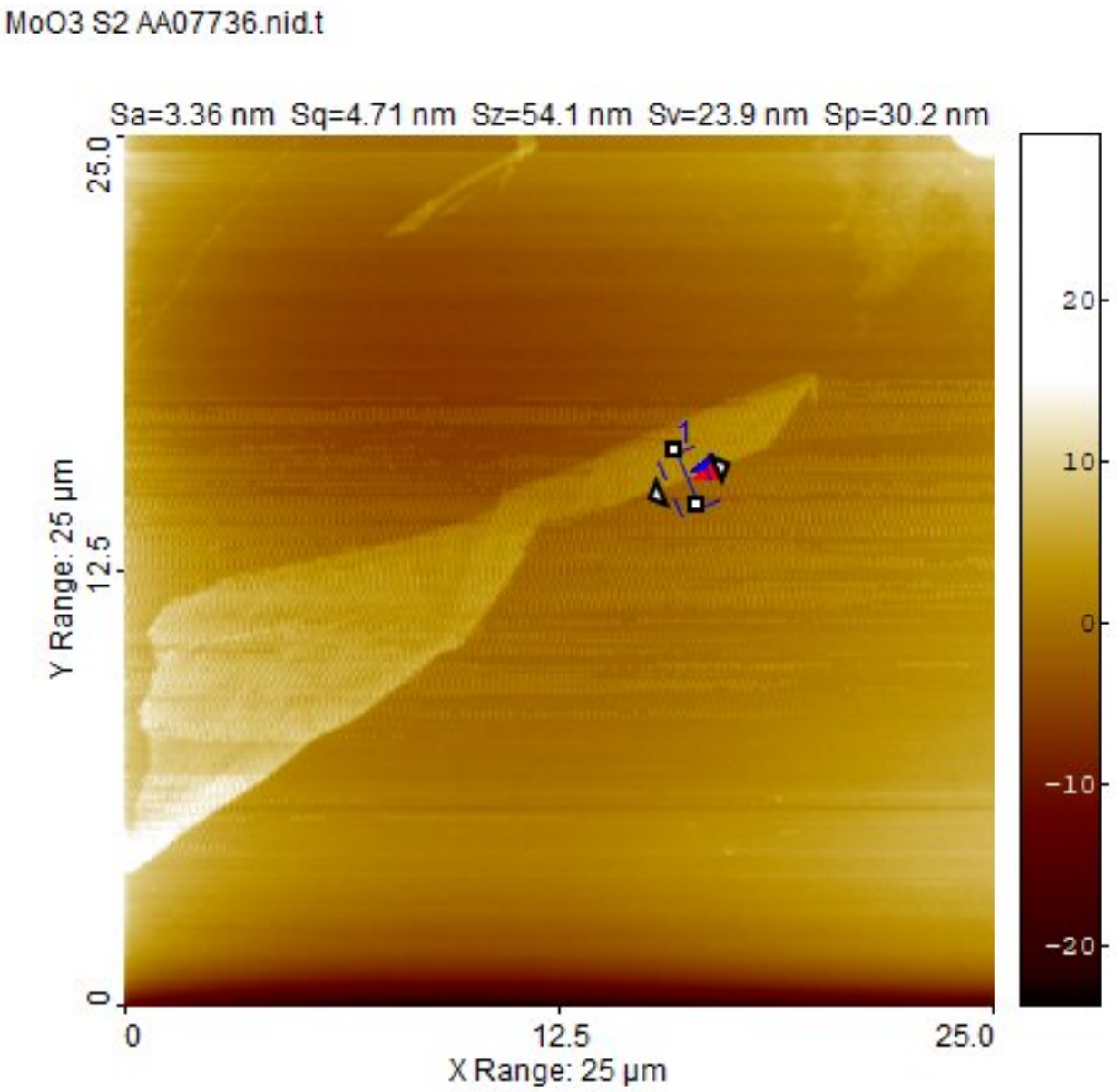

Figure 10: AFM image of the third selected flake. Scan size is 25 micro meter

Corresponding height analysis given below.

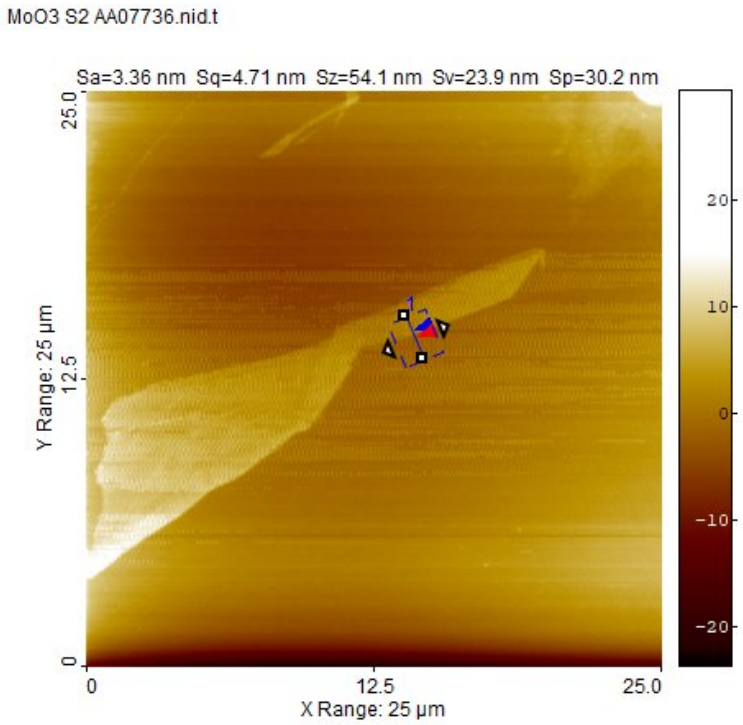

(a) AFM image of the selected flake.

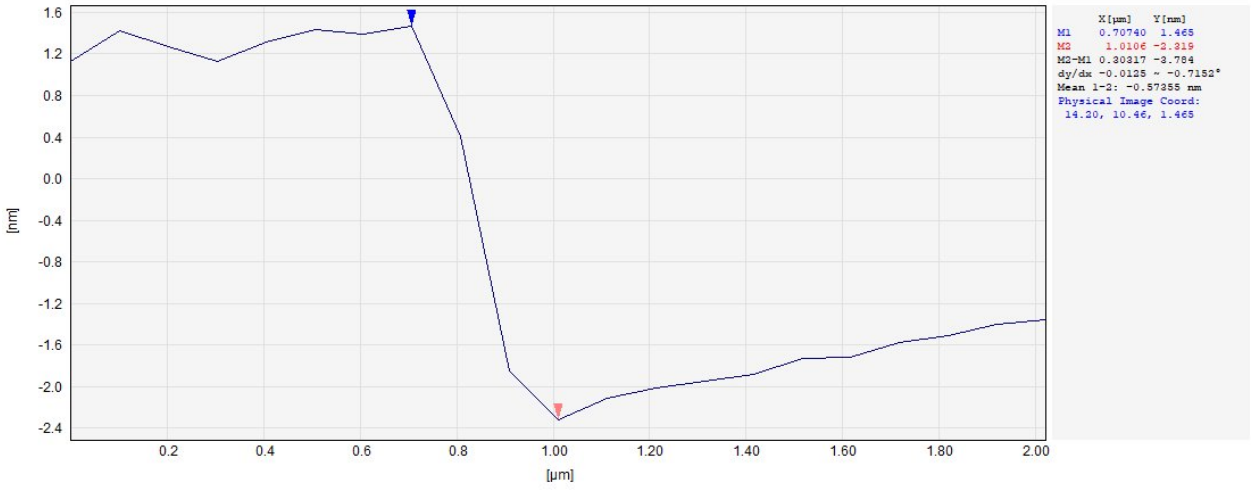

(b) Height analysis corresponding to the AFM image.

Figure 11: AFM image and height analysis of the selected graphene flake.

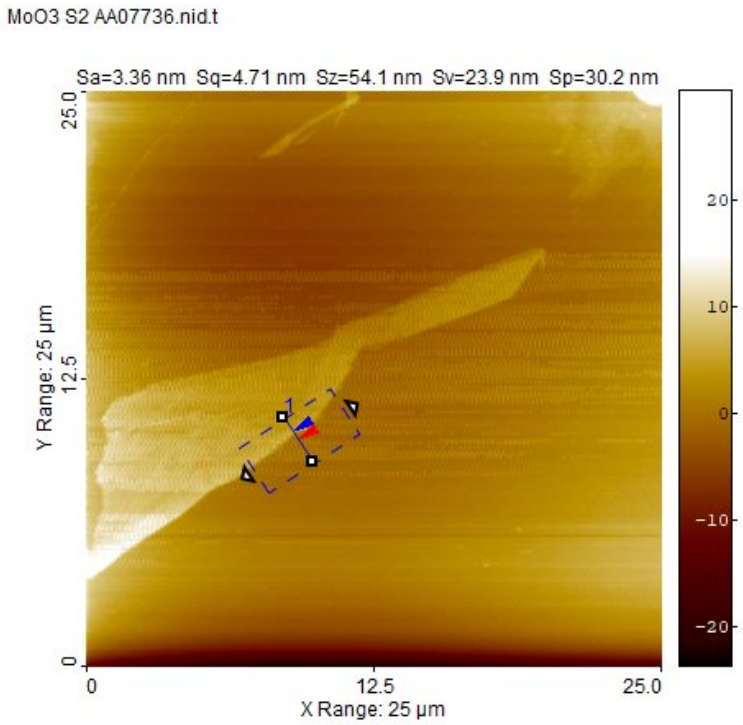

(a) AFM image of the selected flake.

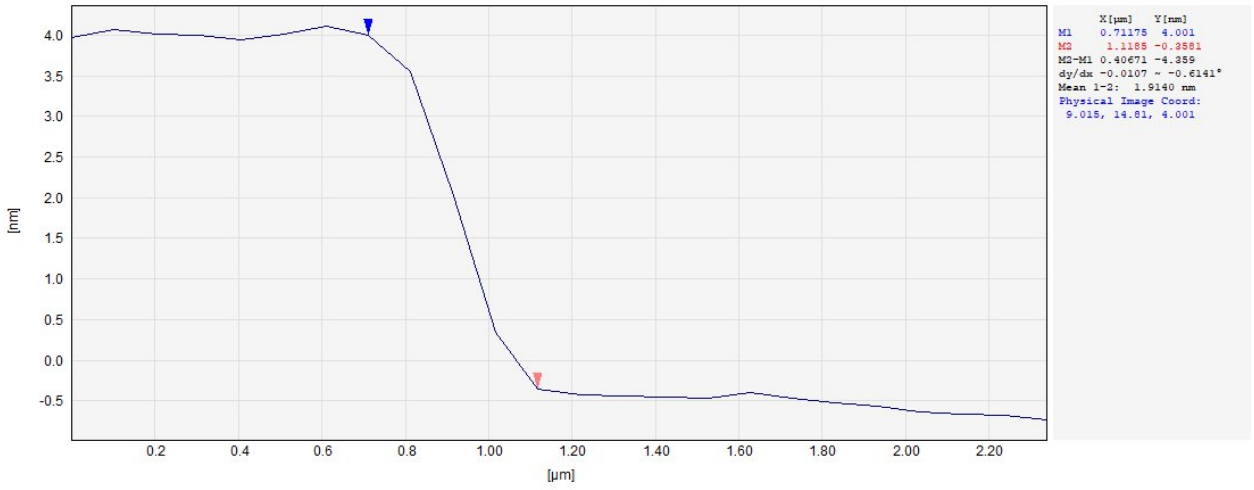

(b) Height analysis corresponding to the AFM image.

Figure 12: AFM image and height analysis of the selected graphene flake.

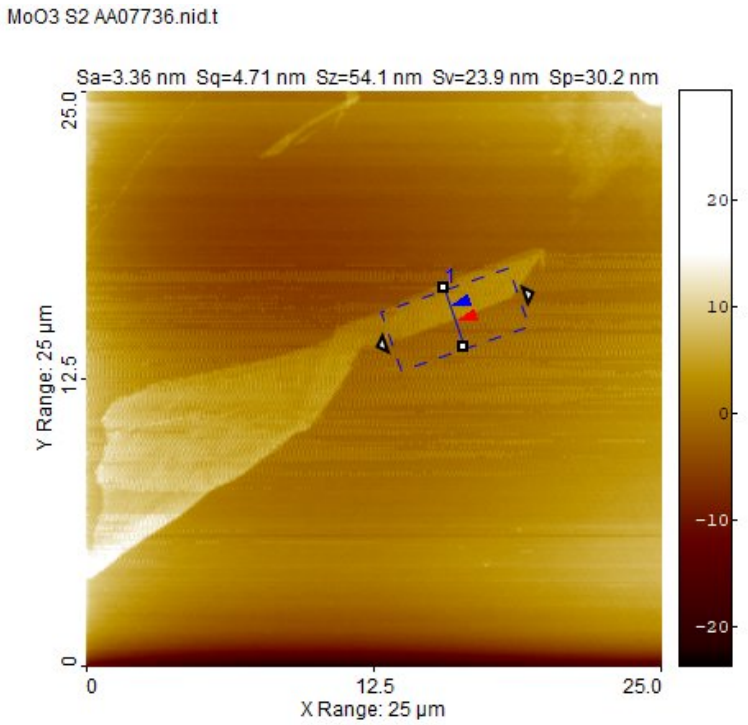

(a) AFM image of the selected flake.

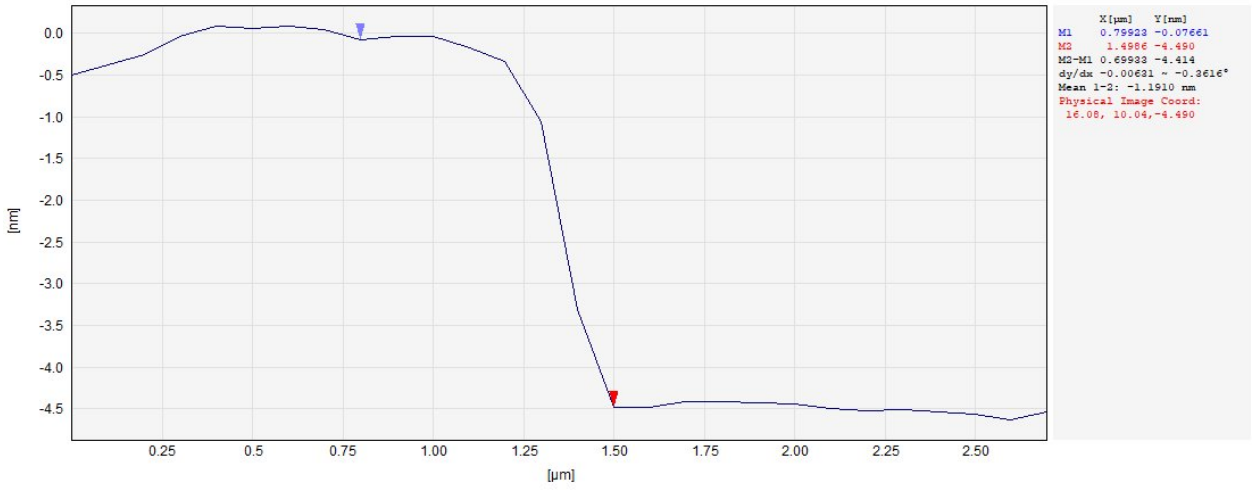

(b) Height analysis corresponding to the AFM image.

Figure 13: AFM image and height analysis of the selected graphene flake.

Despite some noise present in the AFM data, the height measurements across several random locations on the flake exhibited a consistent profile. By averaging these values, a reliable step height of approximately **4 nm** was obtained. Given that a single graphene layer contributes roughly **0.34 nm**,

this corresponds to approximately **12 layers** of graphene. The consistency of the height across different regions, despite image noise, supports this layer estimation and indicates that the flake is a **few-layer graphene structure** rather than a monolayer or thick multilayer.

Chapter 7

Estimation of Number of layers of Graphene using Raman-Spectroscopy

7 Raman Analysis of the Graphene Flakes

Raman analysis was performed on the three previously AFM-characterized flakes and an additional exfoliated flake to determine the number of graphene layers. The corresponding Raman spectra for the four graphene flakes are given below.

7.1 Spectra of the Subsrtate

The Raman spectrum of the bare Si/SiO substrate was recorded separately to identify the characteristic Raman peaks of silicon, particularly the prominent peak around 520 cm^1. This step is essential to distinguish substrate-related signals from the graphene flake signals during spectral analysis, ensuring that the interpretation of the graphene features is not influenced by the underlying silicon background

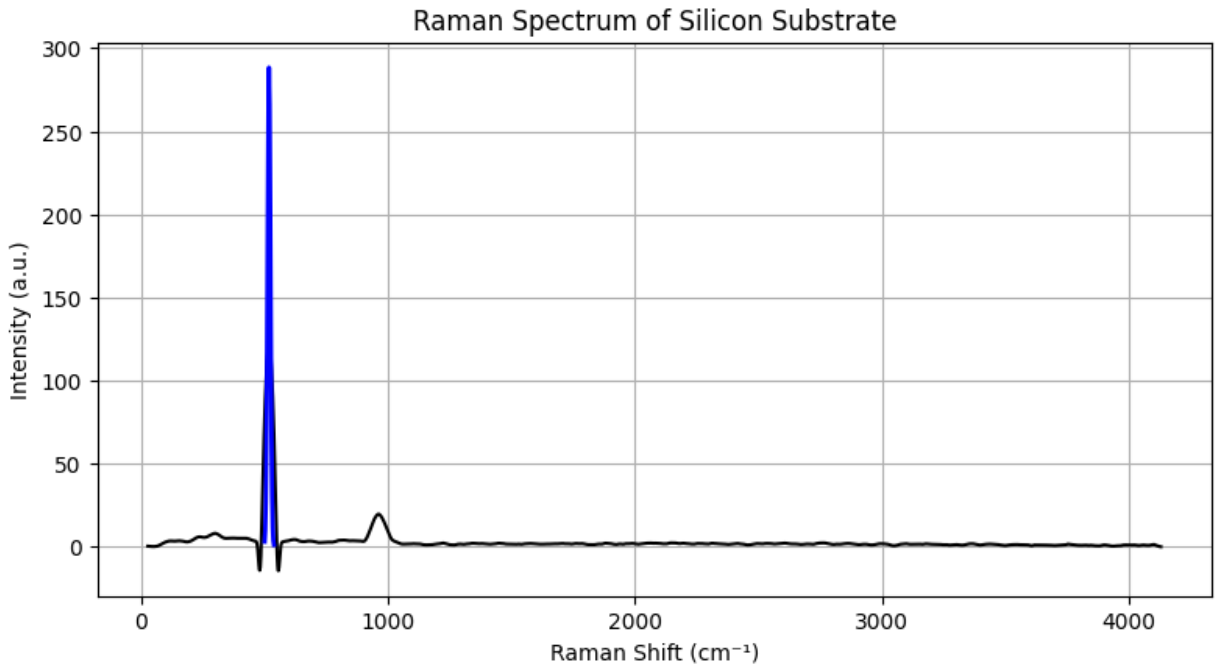

Figure 14: Curve-fitted Raman spectrum of the bare Si/SiO_2 substrate, showing a prominent silicon peak at 520 cm^{-1}. This reference spectrum was used to identify and subtract substrate-related contributions in the analysis of graphene flakes.

7.2 Raman Spectra of Flake 2

Flake 1 was excluded from Raman analysis due to the lack of a reliable height estimate from AFM measurements. Therefore, Raman characterization was carried out starting from Flake 2.

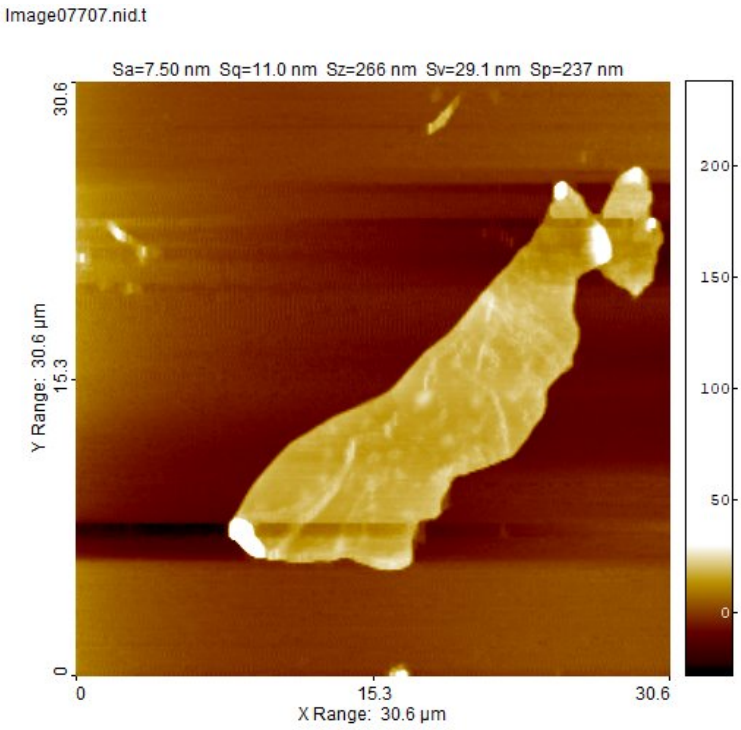

(a) AFM image of the selected flake.

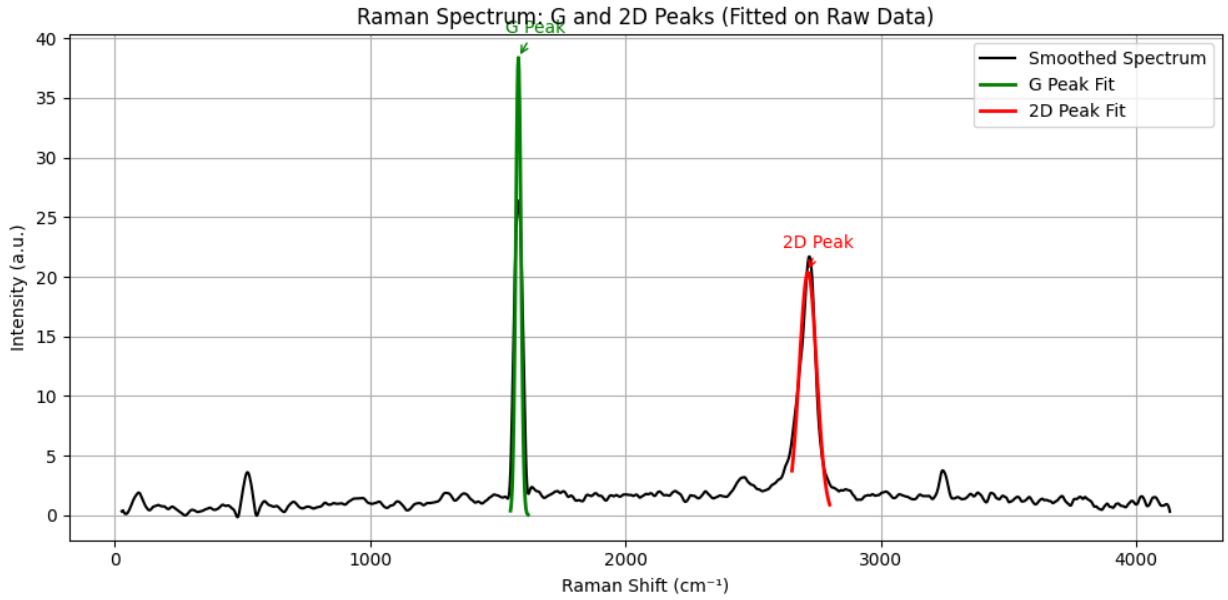

(b) Raman analysis corresponding to the AFM image.

Figure 15: AFM image and Raman spectra analysis of the selected graphene flake.

The Raman peak analysis of Flake 2 reveals characteristic features consistent with multilayer graphene. Atomic Force Microscopy (AFM) mea-

surements indicate a height of approximately 30 nm, which corresponds to nearly 88 layers of graphene. The Raman spectrum shows a prominent G peak at 1581.35 cm^{-1} with an intensity of 41.20, and a 2D peak at 2721.39 cm^{-1} with an intensity of 23.80. The resulting intensity ratio, I(2D)/I(G), is 0.58, which is typical for multilayer graphene and supports the conclusion derived from the AFM data.

7.3 Raman Spectra of Flake 3

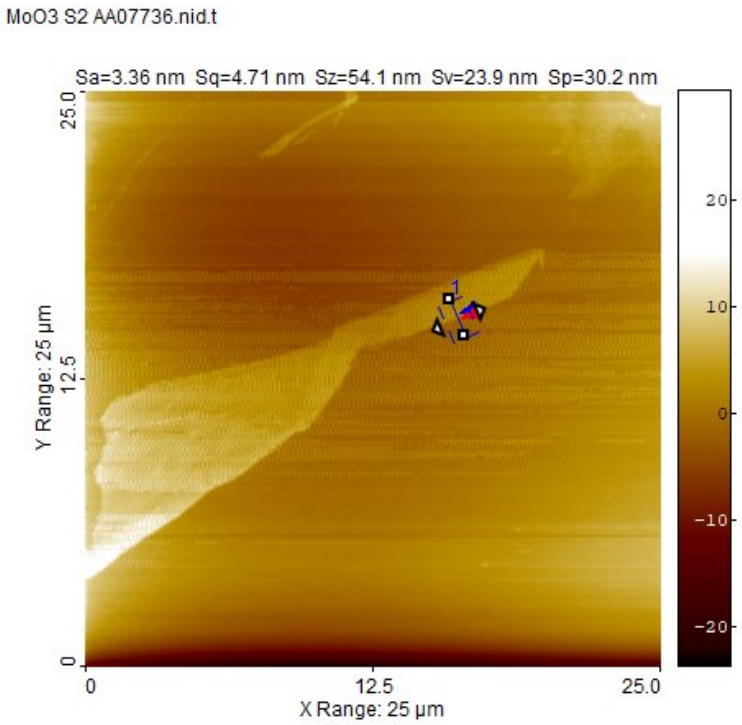

(a) AFM image of the selected flake.

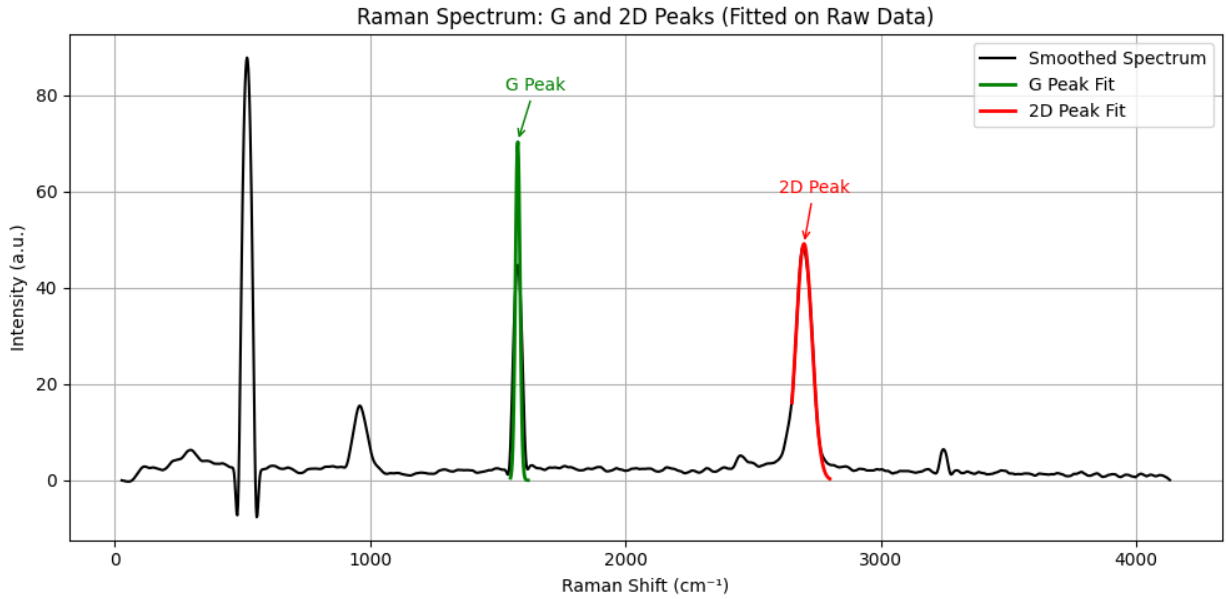

(b) Raman analysis corresponding to the AFM image.

Figure 16: AFM image and Raman spectra analysis of the selected graphene flake.

The Raman analysis of Flake 3, which had an AFM-measured height of approximately 4 nm (indicating around 12 layers), shows characteristics consistent with few-layer graphene. The G peak is observed at 1579.12 cm^{-1} with an intensity of 74.40, while the 2D peak appears at 2694.43 cm^{-1} with an intensity of 50.00. The resulting intensity ratio I(2D)/I(G) is 0.67. This value is typical for few-layer graphene and supports the height-based estimate of approximately 12 layers.

7.4 Raman Spectra of an additional Flake(4)

Another flake, visually identified as thinner than Flake 3 based on optical contrast, was selected for Raman spectroscopy prior to AFM measurement. The Raman spectrum was acquired immediately, and the estimation of the number of layers was carried out using the intensity ratio of the G and 2D peaks. leveraging Raman spectroscopy as a preliminary diagnostic tool in the absence of immediate AFM data.

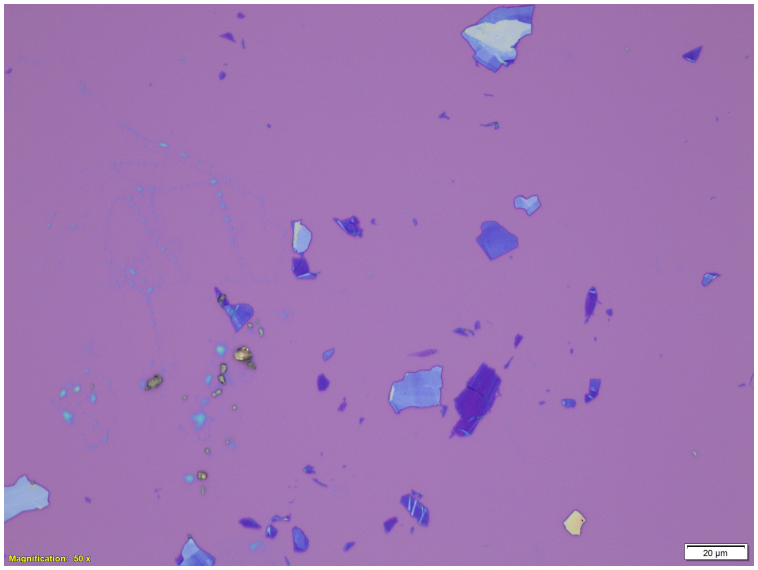

(a) AFM image of the selected flake.

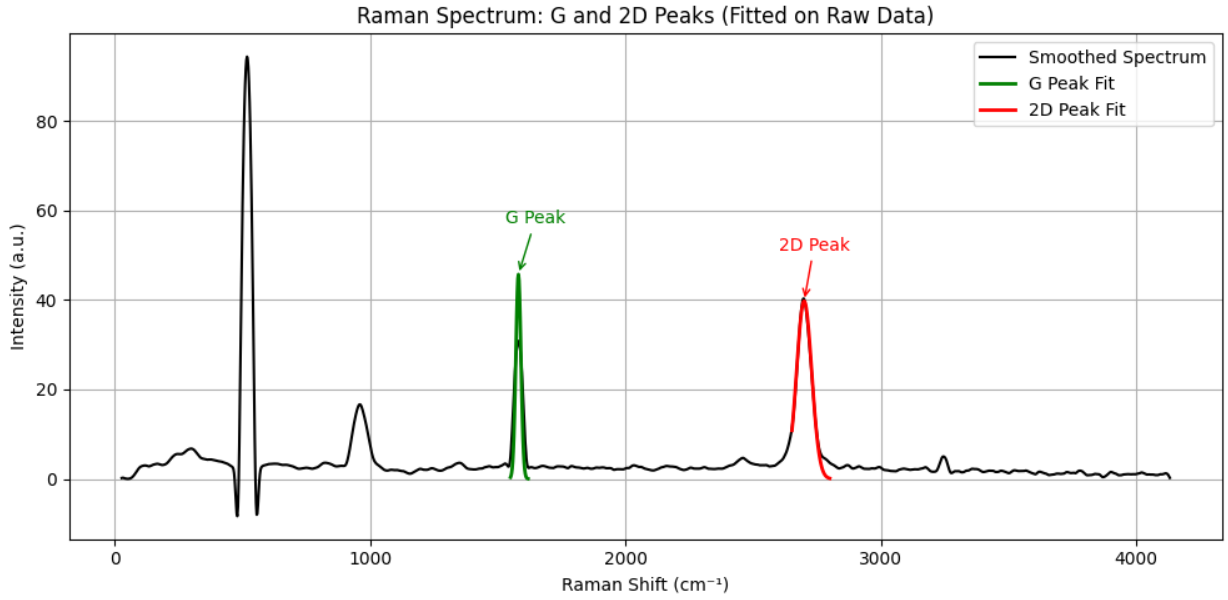

(b) Raman analysis corresponding to the AFM image.

Figure 17: AFM image and Raman spectra analysis of the selected graphene flake.

The Raman spectrum obtained from the thinner flake showed characteristic peaks of graphene. The G peak appeared at 1581.35 cm^{-1} with an intensity of 49.40, while the 2D peak was observed at 2692.50 cm^{-1} with an intensity of 41.80. The resulting intensity ratio $I(2D)/I(G)$ was calculated to be approximately 0.85. This value, combined with the relatively symmetric and sharp nature of the 2D peak, is indicative of few-layer graphene,

most likely bi-layer or tri-layer. While AFM measurements are still pending, the Raman analysis provides strong preliminary evidence that the flake is thinner than Flake 3, which was confirmed to be multi-layer graphene. This estimation further demonstrates the utility of Raman spectroscopy in thickness assessment.

Chapter 8

Conclusion

This internship focused on the study of thin graphene flakes using Atomic Force Microscopy (AFM) and Raman Spectroscopy. The main aim was to identify and analyze few-layer graphene samples.Several flakes were selected and measured using AFM to estimate their thickness. The recorded heights ranged from around 4 nm to 30 nm, which suggests the presence of approximately 12 to 88 layers. These measurements helped narrow down the flakes most likely to be few-layer graphene.

Raman Spectroscopy was then used to examine the same flakes. Key features such as the G and 2D peaks were analyzed. The intensity ratio between these peaks helped estimate the number of layers. In one of the flakes, an I(2D)/I(G) ratio of around 0.85 indicated the presence of bilayer or few-layer graphene. In some cases, Raman analysis was carried out even before AFM measurements when the flake appeared promising by eye. This allowed faster decisions and better use of available lab time. Overall, the work successfully demonstrated how AFM and Raman data together can be used to identify thin graphene layers, and provided hands-on experience with important characterization tools.